Opto-Electronic Advances

CN 51–1781/TN ISSN 2096–4579 (Print) ISSN 2097–3993 (Online)

Highly textured single-crystal-like perovskite films for large-area, high-performance photodiodes

Runkai Liu, Feng Li and Rongkun Zheng

Citation: Liu RK, Li F, Zheng RK. Highly textured single-crystal-like perovskite films for large-area, high-performance photodiodes. *Opto-Electron Adv* **8**, 250168(2025).

https://doi.org/10.29026/oea.2025.250168

Received: 7 July 2025; Accepted: 16 November 2025; Published online: 19 December 2025

Opto-Electronic Advances

Article

December 2025, Vol. 8, No. 12

DOI: 10.29026/oea.2025.250168 CSTR: 32247.14.oea.2025.250168

Highly textured single-crystal-like perovskite films for large-area, high-performance photodiodes

Runkai Liu, Feng Li* and Rongkun Zheng*

Organometallic perovskite single crystals have been considered one of the most promising candidates for photodetection applications, owing to their grain-boundary-free structure and improved optoelectronic properties. However, several challenges still remain for the application of perovskite single crystals in photodetectors, in particular the thickness and area controls and poor compatibility with substrates. Herein, we report a straightforward fabrication process for realizing large-area (up to 100 cm^2) and highly textured single-crystal-like $MAPbBr_3$ films by combining inverse-temperature crystallization with a hot-pressing process. Thanks to the following hot-pressing treatment, the obtained perovskites can be effectively integrated onto the FTO substrates without falling, facilitating electrical connections and device integration. The obtained $MAPbBr_3$ exhibits a low trap density of 1.4×10^{11} cm^{-3} and a high mobility of 217 $cm^2 \cdot V^{-1} \cdot s^{-1}$ (with a high mobility-lifetime product of up to 5.4×10^{-4} $cm^2 \cdot V^{-1}$). The resulting photodiodes exhibit the self-powered capability and show a maximum responsivity approaching 944 $mA \cdot W^{-1}$, a champion detectivity exceeding 10^{11} Jones, and a fast photoresponse of 45 ms, together with excellent stability. This study constitutes a demonstration of highly textured, large-area perovskite photodiodes integrated sturdily onto FTO substrates and paves the way for various practical applications, such as optical imaging technology.

Keywords: large-area; highly textured single-crystal-like halide perovskite; facile synthesis; photodiode device; high responsivity

Liu RK, Li F, Zheng RK. Highly textured single-crystal-like perovskite films for large-area, high-performance photodiodes. *Opto-Electron Adv* **8**, 250168 (2025).

Introduction

Photodetectors function as crucial modules that convert optical signals into electrical information and have become increasingly prevalent due to their widespread applications in the fields of imaging, sensing, and optoelectronic networks[1,2]. The key component of a photodetector is the photo-sensitive medium (in general semiconductor materials or related composites or heterostructures) that acts as a light absorber, generating electrons and holes when excited by incident photons with the suitable energy. So far, various materials with different structures and forms have been employed as the active light-harvesting medium in photodetectors working in different wavelength ranges from ultraviolet (UV) to infrared (IR); mainly, these materials include silicon, germanium, III–V semiconductors, oxide semiconductors, 2D materials, organic molecules, and conjugated polymers[3–6]. Except for these traditional materials, lead (Pb) halide perovskites (with the general formula of $APbX_3$, where A is either the organic cation like MA^+ or inorganic

School of Physics, The University of Sydney, NSW 2006, Australia.

*Correspondence: F Li, E-mail: feng.li2@sydney.edu.au; RK Zheng, E-mail: rongkun.zheng@sydney.edu.au

Received: 7 July 2025; Accepted: 16 November 2025; Published online: 19 December 2025

Cs^+; and X is a halide anion such as Cl^-, Br^- or I^-) have successfully been demonstrated for highly efficient photodetection applications beyond the widely studied photovoltaic and light-emission device applications, owing to their outstanding optoelectronic properties, including large light absorption coefficient[7], long carrier lifetime[8], tunable bandgaps[9], and high optical attenuation[10], as well as low-cost raw materials[11] and facile processing[12]. Notably, as a representative organic-inorganic hybrid perovskite, methylammonium lead bromide ($MAPbBr_3$) also possesses the above-mentioned favorable characteristics; it has been widely researched as the active layer in various optoelectronic devices, in particular photodetectors[13]. Specifically, among various types of hybrid perovskites, $MAPbBr_3$ could offer more favorable properties[14]. For example, $MAPbBr_3$ could exhibit relatively more stability against moisture and oxygen than other perovskites like I-based or FA-based ones[15], while also providing a broader optical absorption range than Cl-based hybrid perovskites[16]. These features result in a balanced combination of lower exciton binding energy, longer carrier diffusion length, improved stability, and broader optical absorption, making $MAPbBr_3$ an excellent material for photodetection applications.

Compared to the halide perovskite polycrystalline films, single-crystal counterparts, due to their highly improved crystallinity and eliminated grain boundaries, present numerous favorable properties, such as larger $\mu\tau$ product, lower trap density, and higher stability[17–19]. Consequently, single-crystal halide perovskites with various forms and dimensions have drawn great attention towards high-performance and highly stable photodetectors[20–23]. It is worth noting that, despite the achieved photodetection performance, the free-standing and bulk perovskite single crystals (obtained through the traditional solution-based methods) and the thin single crystals (normally processed by the space-confined solution-processed method) still suffer from the large thickness and ultrasmall area, respectively. These highly restrict the device fabrication and integration for practical applications. For example, in real-world cases like imaging applications, the photosensitive area is normally required to be comparable to the size of the object. In this sense, improvement strategies of synthesis for large-area single-crystal perovskites with suitable thickness, along with reduced defects and promising optoelectronic properties, are particularly attractive and show an ever-growing demand.

Significant research efforts have been focused on developing effective methods to produce single-crystal perovskites with an optimal balance of controllable size and superior physical properties. Notably, Saidaminov et al. introduced a modified antisolvent vapor-assisted crystallization technique to grow large-area, planar-integrated perovskite single-crystalline films, and these samples exhibit promising carrier mobility and diffusion lengths comparable to those of free-standing perovskite single crystals[24]. Furthermore, the related photoconductors based on these materials demonstrate high photogain, exceeding 10^4 electrons per photon[20]. However, the device performance of photoconductors is often limited by the use of highly conductive channel materials, which present a trade-off between photogain and dark current levels[25]. It should be worth noting that compared with photoconductors, photodiodes stand out due to their potential for achieving high specific detectivity, fast temporal response, broad dynamic range, and color selectivity. Despite these advantages, realizing large-area single-crystal perovskite photodiodes with high photodetection performance and rapid photoresponse speeds remains a significant challenge.

Herein, we report a straightforward and adjusted inverse-temperature crystallization (ITC) method that incorporates additional perturbations from magnetic stirring during crystallization and subsequent hot-processing treatment. This approach enables the synthesis of highly textured, single-crystal-like perovskite films[24] with a large area of up to 10 × 10 cm^2 and a thickness of 145 μm. To our knowledge, this represents the maximum area for single-crystal perovskites so far, with most of the prior examples being normally smaller than 5 × 5 cm^2 [26–30]. (see Tables S1 and S2 for detailed comparisons). Remarkably, the optimized $MAPbBr_3$ exhibits significantly improved optical and electrical properties, including a high charge carrier mobility of up to 217 $cm^2 \cdot V^{-1} \cdot s^{-1}$ and the large $\mu\tau$ product approaching 5.4 × 10^{-4} $cm^2 \cdot V^{-1}$. Leveraging these large perovskites as active light-absorbing materials, along with suitable charge-transporting layers, we successfully fabricated large-area, highly efficient perovskite single-crystal photodiodes. The combination of the perovskite layers' superior electrical properties and the reduced dark current density afforded by the device designs and charge-transporting layers results in the photodiodes showing outstanding performance metrics: a high responsivity of 944 $mA \cdot W^{-1}$, an optimal detectivity of up to 1 × 10^{11} Jones, and a fast photoresponse of 45

ms, along with excellent stability. These findings highlight a pathway toward low-cost, high-performance photodiodes with significant potential for real-world applications.

Results and discussion

Growth of large-area highly textured single-crystal-like perovskites

The large-area, highly textured single-crystal-like $MAPbBr_3$ samples were synthesized via an adjusted inverse temperature crystallization (ITC) technique, incorporating several key modifications. Specifically, the optimized group undergoes a temporal temperature gradient, where the temperature is increased at a rate of 5 °C per hour, followed by hot pressing. In contrast, the control group is processed using the traditional heating crystallization at a fixed high temperature without hot pressing treatment. Besides, additional perturbations were introduced during the crystallization process, as schematically shown in Fig. 1(a). The perturbations, triggered by stirring a magnetic bar in the perovskite precursor solution, would facilitate the generation of high-density and uniform perovskite single-crystal seeds, enabling the coverage of large-area substrates with uniform, highly textured single-crystal-like perovskite. The synthesis process began by immersing a fluorine-doped tin oxide (FTO)/glass substrate into the $MAPbBr_3$ precursor solution while gradually increasing the temperature and stirring the magnetic bar (Step 1). This could induce the nucleation and growth of highly textured single-crystal-like perovskites. Once the crystals grew sufficiently to interconnect and uniformly cover the entire FTO/glass substrate, the obtained highly textured single-crystal-like samples were removed from the precursor solution. The resulting highly textured single-crystal-like perovskite was then annealed on a hot plate to eliminate residual solution (Step 2). Remarkably, large-area, highly textured single-crystal-like perovskites were obtained within just six hours; notably, this is a significant improvement over the previously reported methods[31,32]. To further enhance the quality of the highly textured single-crystal-like perovskites, the as-synthesized samples underwent thermal pressing treatment under a 2 kg weight on a hot plate for six hours (Step 3). This process smoothed the surface of perovskite single-crystal samples and effectively reduced voids within the samples. Consequently, a uniform, highly textured perovskite sample composed of integrated single crystals with a maximum area of up to 100 cm^2 can

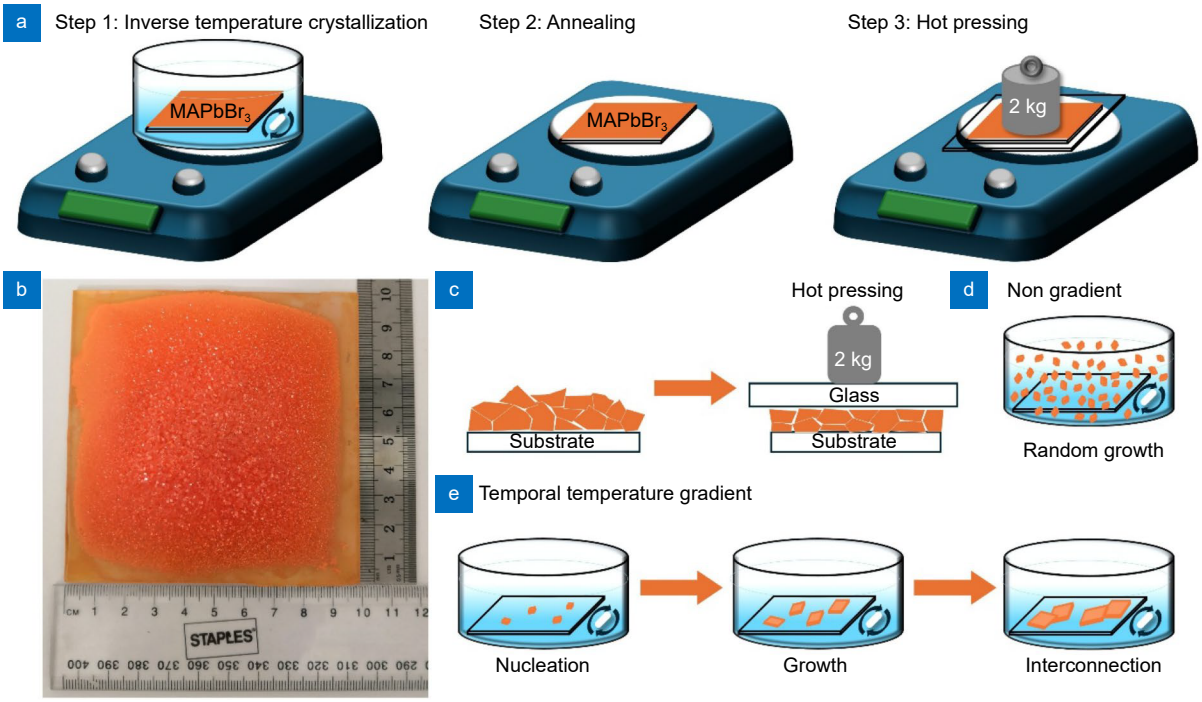

Fig. 1 | (**a**) Step-by-step schematic illustration for the fabrication of highly textured, large-area single-crystal-like $MAPbBr_3$. (**b**) Photograph of the obtained 10 × 10 cm^2 highly textured single-crystal-like $MAPbBr_3$. (**c**) Schematic illustration showing the strategy for improving the morphology of highly textured $MAPbBr_3$ crystals with hot-pressing treatment. Crystallization mechanisms of perovskite samples for (**d**) random growth at high temperature and (**e**) oriented growth under a temporal temperature gradient.

be obtained in Fig. 1(b), which is termed as single-crystal-like perovskite in our work. The hot-pressing treatment could also significantly improve the compatibility between the highly textured single-crystal-like perovskite and the substrate, as shown in Fig. 1(c). Mechanical stability tests demonstrated that the highly textured single-crystal-like perovskite integrated on the FTO/glass substrate could support a 44 g wrench and its own weight without delaminating or sustaining damage (Fig. S1(a)). In contrast, highly textured single-crystal-like perovskites without hot-pressing treatment could detach or break under the same conditions (Fig. S1(b)).

We would highlight that, unlike the conventional ITC method, several key modifications were introduced to enhance the synthesis process in our case. Specifically, a magnetic stirrer was employed in the perovskite precursor solution to create a perturbed environment. The introduced perturbations could facilitate the formation of a uniform, high-density of single-crystal perovskite seeds, sufficient for forming large-area, uniform, highly textured single-crystal-like perovskite active layers to cover the large substrates. From the aspect of crystallography, this perturbation can also lead to the fluctuation of solid particle size and improve the possibility of nucleation, which means that the nucleation site will be increased, so it is more likely to enlarge the surface area and further cover the whole surface of the large-size substrate[33]. In the traditional ITC process, adjacent perovskite nuclei grow until they merge into a continuous structure[34,35]. To evaluate the impact of our modification, we conducted a comparative experiment using the conventional ITC method without using a magnetic stirrer. As shown in Fig. S2, the synthesized perovskite sample exhibited irregular grain sizes and a highly rough sample surface. Additionally, the retrieved sample displayed poor quality, characterized by non-uniformity, fragility, and delicate structural integrity. In contrast, using our modified ITC method, incorporating mild perturbation, could lead to the formation of uniform and interconnected perovskites with a large area, fully covering the large-size FTO/glass substrate.

The introduced perturbation, generated by using the magnetic stirrer, can also increase perovskite nucleation sites, thereby promoting the growth of highly textured single-crystal-like perovskites. During crystallization, we gradually increased the temperature by 5 °C per hour, starting from 80 °C. Figure S3(a) shows that the solution remained clear throughout the process, with halide perovskite precipitating slowly onto the FTO/glass substrate as the temperature increased. In contrast, a rapid temperature rise led to a turbid solution, because the small $MAPbBr_3$ single-crystal seeds could be formed evenly throughout the solution (Fig. S3(b)). These small crystals eventually settled onto the substrate, resulting in less controlled growth of perovskite single crystals. This phenomenon occurs because a rapid temperature increase exceeds the critical free energy threshold for nucleation, triggering the simultaneous formation and growth of numerous perovskite crystals[36]. As illustrated in Fig. 1(d), this process results in grain refinement and random crystallization, with randomly oriented crystals accumulating on the FTO/glass substrate. This makes it challenging to control the orientation of the resulting perovskite samples[37]. In contrast, the gradual temperature increase in our modified method allowed the perovskite single crystals to form preferentially onto the substrates, undergoing nucleation, growth, and interconnection (Fig. 1(e))[38,39]. As the temperature continued to rise, the large-area, highly textured single-crystal-like $MAPbBr_3$ can form, exhibiting a well-controlled orientation and uniform thickness. These prove that the gradual and controlled temperature increase is essential for achieving high-quality, large-area, highly textured single-crystal-like perovskites.

Structural characterization of highly textured single-crystal-like perovskites

To verify the excellent crystallinity of the synthesized large-size, highly textured single-crystal-like perovskite, we conducted X-ray diffraction (XRD) measurements to analyze their crystalline properties. The obtained XRD pattern of the perovskite sample without both the hot-pressing and temperature-gradient treatments (Fig. 2(a)) reveals several miscellaneous diffraction peaks, in addition to the primary peaks (such as (100), (200), and (300)) seen in the optimized sample. These additional peaks (including (110), (210), (211), and (220)) indicate random crystallization, where the random orientation of crystals arises from the lack of a temporal temperature gradient. In contrast, the optimized perovskite sample exhibits only the main peaks (including (100), (200), and (300)), demonstrating significantly improved crystal orientation due to the applied additional treatments. Moreover, no changes in the XRD patterns were observed after 2 months of aging, indicating excellent material stability.

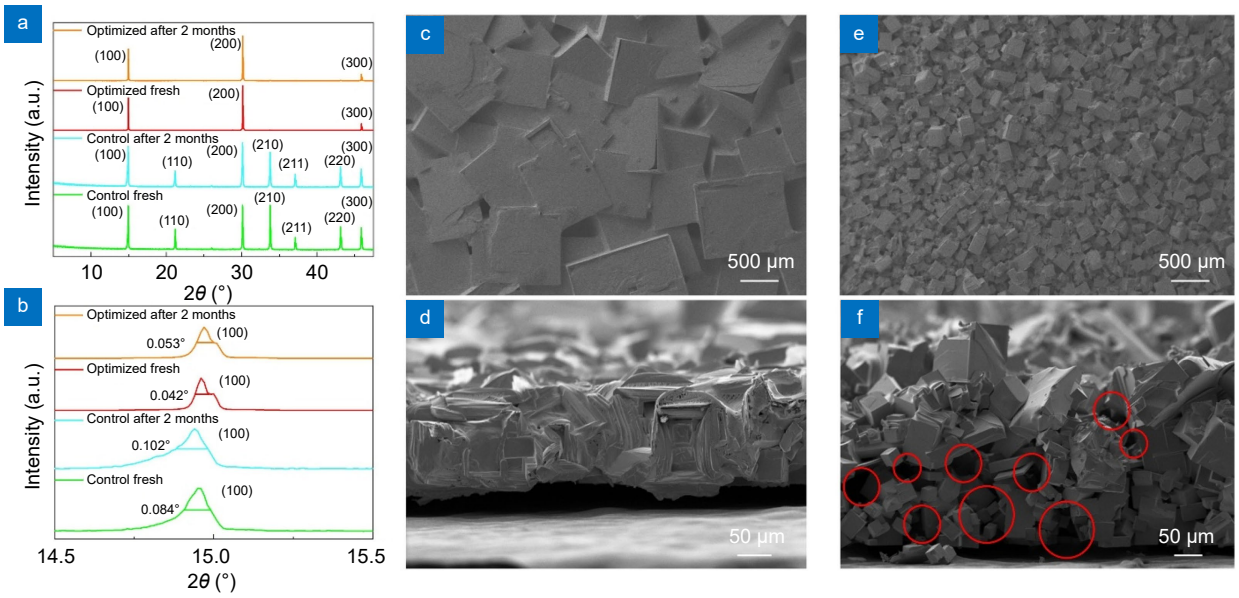

Fig. 2 | (**a**) XRD patterns of the control and optimized highly textured single-crystal-like $MAPbBr_3$ perovskites, including the optimized sample after 2 months of storage in a nitrogen-filled glove box at room temperature for stability testing. (**b**) Comparison of FWHM values for control and optimized $MAPbBr_3$ perovskites, as well as the optimized sample after 2 months of storage, highlighting differences in crystallinity and stability. (**c**) SEM image showing the surface morphology of the optimized highly textured single-crystal-like $MAPbBr_3$, treated with a hot-pressing process and a temporal temperature gradient (scale bar = 500 μm). (**d**) Cross-sectional SEM image of the optimized $MAPbBr_3$ showing uniform thickness and tightly interconnected crystals (scale bar = 50 μm). (**e**) SEM image showing the surface morphology of the control $MAPbBr_3$, synthesized without hot pressing or a temporal temperature gradient, indicating smaller grains and rougher texture (scale bar = 500 μm). (**f**) Cross-sectional SEM image of the control $MAPbBr_3$, revealing increased thickness, pinholes, and uneven morphology (scale bar = 50 μm).

Furthermore, the full width at half maximum (FWHM) of the XRD peaks for the optimized perovskite is 0.042°, markedly narrower than the value of 0.084° observed in the control sample, indicating superior crystallinity and reduced grain refinement under the temperature-gradient treatment (Fig. 2(b)). XRD tests after 2 months of storage further confirmed the high stability of the optimized perovskites; that is, even after two months of storage in a glove box at room temperature under a nitrogen atmosphere, no additional diffraction peaks appeared. This clearly suggests excellent phase stability of the optimized highly textured single-crystal-like perovskite. The FWHM of the optimized sample after storage increased slightly to 0.053°, compared to the value of 0.042° for the fresh sample. Conversely, the FWHM of the control sample increased significantly to 0.102° from 0.084° in the fresh sample. These further emphasize the enhanced stability of the optimized highly textured single-crystal-like perovskites.

To further elucidate the effects of the temporal temperature gradient and hot-pressing treatments, surface morphology and cross-sectional features of the perovskite samples were analyzed using scanning electron microscopy (SEM) measurements. Hot pressing has been proven to be an effective method for enhancing the quality of various types of thin films and single crystals by minimizing defects, controlling voids, and achieving a smoother surface[40]. The SEM image as shown in Fig. 2(c) reveals that the optimized highly textured single-crystal-like perovskite samples exhibit uniform crystal orientations, a direct result of the hot-pressing treatment during the crystallization process. These observations align with the XRD findings, confirming the high quality of our highly textured perovskite samples, exhibiting single-crystal-like features. Additionally, the crystal size of the optimized perovskite samples is significantly larger compared to that of the control samples. Larger grains reduce grain boundaries, minimizing defects in the perovskite layer, which is crucial for enhancing photodetection performance[41]. Conversely, the control sample shows clear evidence of grain refinement (Fig. 2(e)), with smaller grains and more grain boundaries. Grain size distribution analysis (Fig. S4) shows that over 70% of grains in the optimized sample range between 600–900 μm, with an average size of up to 771 μm. In comparison, the control sample primarily comprises grains smaller

than 150 μm, with an average size of only about 100 μm.

Hot pressing also plays a critical role in controlling the thickness of the perovskite samples. The cross-sectional SEM image of the optimized perovskite sample (Fig. 2(d)) reveals a uniform thickness of approximately 145 μm, while the control sample (Fig. 2(f)) exhibits a significantly greater thickness of about 400 μm, more than double that of the optimized sample. Furthermore, the optimized perovskite sample demonstrates a relatively smooth and uniform morphology, which can be attributed to the hot-pressing treatment. The control perovskite sample displays a much rougher surface with irregular height variations. A detailed examination of the cross-sectional SEM images highlights the structural differences. The hot-pressed perovskite sample shows tightly interconnected single crystals with no pinholes, ensuring highly improved sample quality. In contrast, the control sample contains small-sized crystals and pinholes among them, as indicated by the red circles marked in Fig. 2(f). The presence of these pinholes would highly affect the optoelectronic and charge-transport properties of the control perovskite samples. Energy-dispersive spectroscopy (EDS) mapping (Fig. S5) further confirms the uniform distribution of all elements in the highly textured single-crystal-like $MAPbBr_3$ after the hot-pressed treatment.

These findings underscore the importance of combining the temporal temperature gradient and hot-pressing strategies. The temperature gradient promotes anisotropic crystallization, suppresses grain refinement, and reduces defects within the obtained highly textured single-crystal-like perovskite[41,42]. Meanwhile, hot pressing could be beneficial for smoothening the sample surface and improving the interface quality between the perovskite samples and the electrodes, thus improving the detector performance and stability[43,44]. Overall, the optimized perovskite sample exhibits ideal crystallinity, size, thickness, and morphology characteristics, which can be attributed to the applied treatments during crystallization. The key effects of these innovations are further summarized in Table 1 for clarity.

Optical and electrical properties of highly textured single-crystal-like perovskites

We then tune to the physical properties of the obtained perovskite samples. We investigated the UV-Vis absorption and photoluminescence (PL) properties of the optimized highly textured single-crystal-like perovskite samples. As shown in Fig. 3(a), the absorption spectrum indicates that the optimized perovskite sample has an absorbance wavelength cutoff around 560 nm. The corresponding bandgap of the optimized $MAPbBr_3$ sample was determined to be 2.23 eV using the Tauc equation: $(\alpha h\nu)^2 = A(h\nu - E_g)$, where α is the absorption coefficient, A is a constant, $h\nu$ is the incident energy, and E_g stands for the material's bandgap (Fig. 3(b))[45]. The steady-state PL spectrum exhibits a peak at approximately 550 nm, with a full width at half maximum (FWHM) of about 19.5 nm, consistent with previously reported publications[46]. These results reflect the high crystallinity and optical quality of the optimized highly textured single-crystal-like perovskite. Additionally, the small difference between the absorption edge and the PL peak suggests minimal vibronic relaxation[47].

To evaluate the homogeneity of the optimized large-sized and highly textured single-crystal-like perovskite samples, we also measured the PL spectra of the samples

Table 1 | Summary of the purposes and effects of innovations for the synthesis of the optimized highly textured single-crystal-like perovskites.

Innovations	Purposes	Effects
Magnetic stirring	Create a perturbed environment during nucleation.	Enhanced density and uniformity of single-crystal seeds, resulting in uniform coverage.
Temporal temperature gradient	Slow the crystallization process. Control nucleation and growth of crystals. Enlarge grain size. Induce anisotropic crystallization.	Reduced random crystallization and improved orientation and texture. Enlarged grains and reduced defects. Improved stability.
Hot pressing	Decrease voids. Flatten the surface. Limit defects.	Larger grains. Fewer defects. Better grain interconnection. Reduced thickness. Enhanced morphology. Well-control orientation Benefit electrode deposition

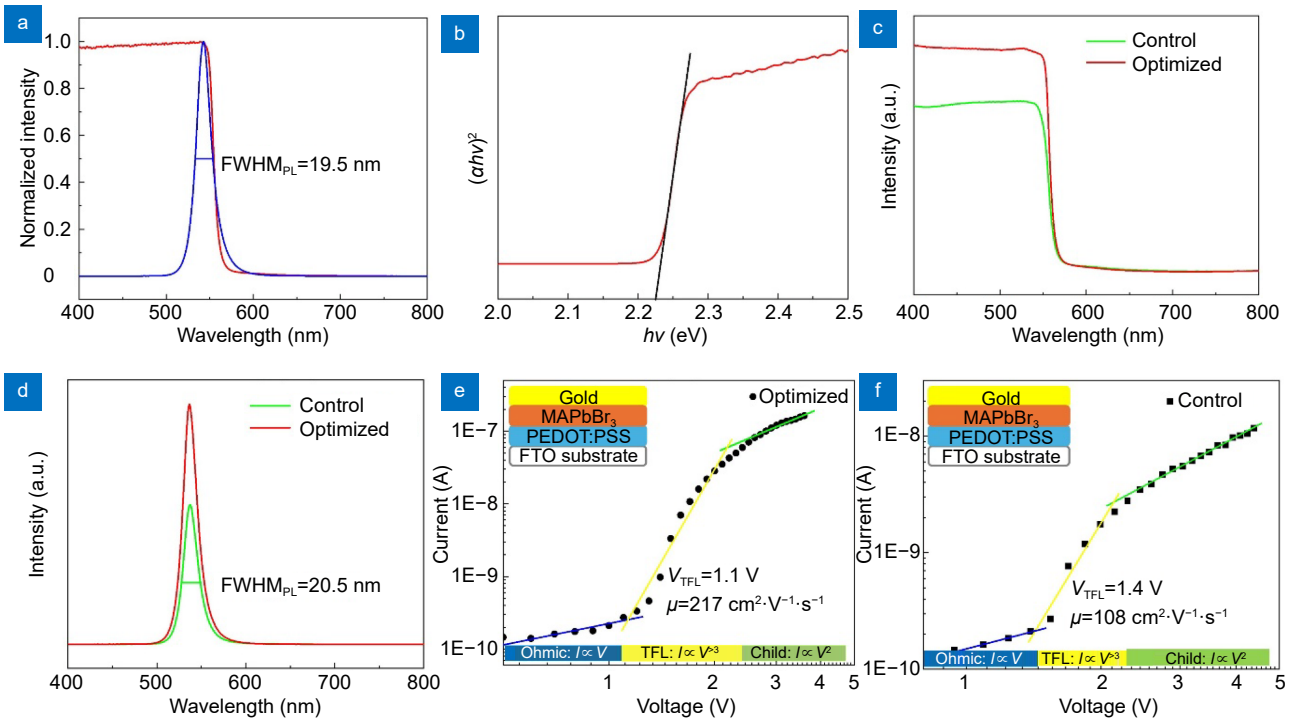

Fig. 3 | (**a**) UV-Vis absorption and steady PL of the optimized highly textured single-crystal-like $MAPbBr_3$. (**b**) Tauc plot for the bandgap of the optimized highly textured single-crystal-like $MAPbBr_3$. (**c**) UV-Vis absorption and (**d**) steady-state PL of the control and optimized highly textured single-crystal-like $MAPbBr_3$ for the comparison of their optical properties. SCLC measurements for (**e**) the optimized highly textured single-crystal-like $MAPbBr_3$ and (**f**) the control highly textured single-crystal-like $MAPbBr_3$, respectively, from which the trap density and carrier mobility can be obtained.

at different sample locations (Fig. S6(a)). The near-identical PL intensities across different areas highlight the uniformity of the optimized $MAPbBr_3$ single-crystal samples, even with large areas. In contrast, the control $MAPbBr_3$ sample shows significant variations in PL intensity across different regions (Fig. S6(b)), consistent with the observed non-uniform cross-sectional morphology (Fig. 2(f)). These measurement results further demonstrate the uniformity of the optimized single-crystal perovskite sample even with a large area, which would be beneficial for high-performance large-sized devices for practical applications.

The stability of the optimized perovskite samples was also assessed through the PL analysis, comparing fresh samples to those stored in a nitrogen-filled glove box at room temperature for 2 months. As shown in Fig. S7, the PL intensity remains nearly unchanged, confirming the exceptional stability of the optimized highly textured single-crystal-like perovskites. These results align with the XRD data as shown in Fig. 2(a), reinforcing the superior stability of the optimized perovskite samples.

Compared with the optimized highly textured single-crystal-like $MAPbBr_3$, the control $MAPbBr_3$ sample exhibited relatively poor performance in both absorption and PL spectra. Figure 3(c) reveals a less steep absorption rise and lower overall intensity for the control sample. Similarly, the PL intensity of the control perovskite sample is markedly reduced compared to the optimized sample (Fig. 3(d)). The FWHM of the PL spectrum for the control sample, measured at 20.5 nm, is broader than that of the optimized perovskite, indicating inferior optical properties. These unsatisfactory optical performances can be attributed to the uneven surface and high trap density of the control $MAPbBr_3$. To be specific, the high trap density will lead to increased trap-assisted carrier recombination, which is nonradiative recombination and undermines the photoluminescence intensity eventually[48].

To predict the photodetection performance of the optimized highly textured single-crystal-like perovskite samples, we investigated their electrical properties using current-voltage (*I-V*) measurements via the space-charge-limited current (SCLC) analysis. This method enabled us to deduce the trap density and carrier mobility of the $MAPbBr_3$ samples[49]. Hole-only devices with the structure of FTO/PEDOT: PSS/optimized (or control)

single-crystal $MAPbBr_3$/Au were fabricated for *I-V* measurements and SCLC analyses. In SCLC analysis, the *I-V* curve typically exhibits three regions: (I) Ohmic region: $I \propto V^1$, which allows the calculation of conductivity. (II) Trap-filling region: the sharp current rise ($I \propto V^n, n > 3$) defines this region, with the trap-filled limit voltage (V_{TFL}) at the intersection with the Ohmic region. Trap density ($N_{trap} = 2\varepsilon\varepsilon_0 V_{TFL}/qL^2$, where $\varepsilon_0 = 8.854 \times 10^{-14}$ F·cm^{-1} is the vacuum permittivity), $\varepsilon = 25.5$ is the relative dielectric constant of $MAPbBr_3$), q is the elemental charge, and L is the thickness of the highly textured single-crystal-like perovskite[50–52]. (III) Child's region: $I \propto V^2$, and carrier mobility (μ) is calculated using the Mott-Gurney law: $J = 9\varepsilon\varepsilon_0\mu V^2/8L^3$, where J and V stand for the current density and applied voltage bias, respectively, and μ and L are the carrier mobility and thickness of the highly textured single-crystal-like $MAPbBr_3$ sample, respectively[53].

From the Ohmic region, the conductivity of the optimized perovskite was determined as 6×10^{-8} Ω^{-1}·cm^{-1}, which is similar to the results from prior research on free-standing single-crystal $MAPbBr_3$[54]. The trap density of the optimized highly textured single-crystal-like $MAPbBr_3$ was calculated as 1.4×10^{11} cm^{-3} (Fig. 3(e)), significantly better than polycrystalline perovskites (9.51×10^{15} cm^{-3}) and comparable to free-standing single crystals (normally with the average value of 7×10^{10} cm^{-3})[55,56]. This low trap density corroborates the improved PL performance (Fig. 3(d)), as high trap densities typically degrade luminescence[57]. The carrier mobility of the optimized highly textured single-crystal-like $MAPbBr_3$ is determined as up to 217 cm^2·V^{-1}·s^{-1} from the fitting of *I-V* data in the Child's region. However, as shown in Fig. 3(f), the carrier mobility of the control $MAPbBr_3$ is approximately 108 cm^2·V^{-1}·s^{-1}, which is only half of that of the optimized one. These results underscore the effectiveness of the temporal temperature gradient and hot-pressing post-treatment in enhancing the quality and electrical properties of our optimized highly textured single-crystal-like perovskite.

Photodiodes based on highly textured single-crystal-like perovskites

The above characterizations demonstrate that the optimized highly textured single-crystal-like $MAPbBr_3$ samples exhibit exceptional optoelectronic properties, including promising optical features, high carrier mobility, and low trap density, making them promising candidates for high-performance photodiodes. To validate this, we fabricated photodiode devices with the vertical structure of FTO/PEDOT:PSS/$MAPbBr_3$/PCBM ([6,6]-phenyl-C61-butyric acid methyl ester)/Ag, as shown in Fig. 4(a). The vertical configuration was chosen because the device thickness of 145 μm is significantly smaller than the average grain size of 771 μm. This ensures that photo-induced charge carriers can travel vertically within the single-crystal perovskite active layer without encountering grain boundaries, thereby reflecting the intrinsic properties of the perovskite layers.

The energy levels of the contained layers in the photodiode device are presented in Fig. 4(b), in which PEDOT:PSS and PCBM layers work as the suitable hole- and electron-transporting layers, respectively. The introduced hole-transporting and electron-transporting layers are beneficial for efficient charge carrier transfer within the fabricated photodiode devices, owing to their matching band alignments with those of the highly textured single-crystal-like $MAPbBr_3$ active layer[58–60]. Specifically, there is a significant energy barrier for hole transfer from the valence band (VB) of $MAPbBr_3$ (−5.6 eV) to FTO (with the work function of −4.4 eV)[59,61]. In the meantime, the VB of PEDOT:PSS at −5.2 eV provides an intermediary step that facilitates the smoother hole transfer[62]. Similarly, the conduction band (CB) of the PCBM at −3.9 eV lies between the CB of $MAPbBr_3$ (−3.4 eV) and the work function of Ag (−4.3 eV), assisting in the efficient transfer of electrons[63]. Additionally, since the VB of PCBM (−5.9 eV) is lower than that of $MAPbBr_3$ (−5.6 eV), the PCBM layer selectively conducts electrons while blocking holes. These energy alignments ensure efficient charge carrier transfer and enhance the overall performance of the resulting photodiodes[64]. To confirm the energy alignments between our sample and the carrier transport layers, we measure the valence band (VB) of the highly textured single-crystal-like $MAPbBr_3$ under zero-bias conditions. Figure S8 presents the UPS analysis of our $MAPbBr_3$ sample, and we can obtain the valence band of −5.24 eV, determined by fitting the tangent to the leading edge of the spectrum[65]. Given the bandgap of 2.23 eV, calculated from the optical absorption data (Fig. 3(b)), the conduction band (CB) can be calculated to be −3.01 eV. The values are in close agreement with the theoretical data and are consistent with the previous reports, further confirming the successful energy alignment.

The mobility-lifetime $\mu\tau$ product is a significant

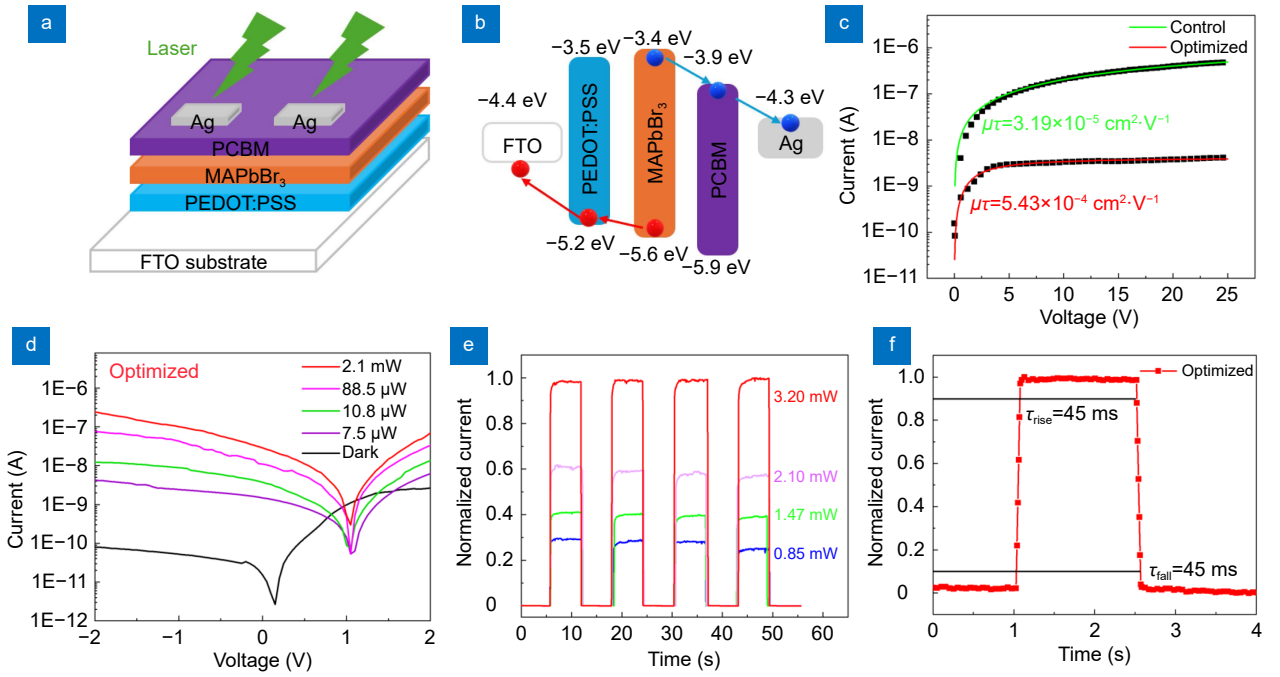

Fig. 4 | (**a**) Device structure of photodiode based on highly textured single-crystal-like $MAPbBr_3$ film. (**b**) Energy-level alignment of each layer in the device. (**c**) Bias-dependent photoconductivity of the control and optimized highly textured single-crystal-like $MAPbBr_3$. (**d**) Current-Voltage curves of the photodiode based on the optimized highly textured single-crystal-like $MAPbBr_3$ in the dark and under laser illumination with different powers. (**e**) Transient photocurrent of the optimized highly textured single-crystal-like $MAPbBr_3$ photodiode under various laser powers of 3.2 mW, 2.1 mW, 1.47 mW, and 0.85 mW. (**f**) Response time of optimized highly textured single-crystal-like $MAPbBr_3$ photodiode.

parameter to assess how far the charge carrier can travel inside the semiconductors, which can be calculated by the Hecht equation: $I = \frac{I_0 \mu\tau V}{L^2}(1 - \exp(-\frac{L^2}{\mu\tau V}))$, where I_0 and $\mu\tau$ are the saturated photocurrent and the mobility-lifetime product that we need to fit, and V and L are the bias voltage and thickness of the highly textured single-crystal-like $MAPbBr_3$, respectively[66]. Therefore, as shown in Fig. 4(c), the $\mu\tau$ product of the control highly textured single-crystal-like $MAPbBr_3$ is extracted as 3.19 × 10^{-5} $cm^2 \cdot V^{-1}$, but that of the optimized highly textured single-crystal-like $MAPbBr_3$ is up to 5.43 × 10^{-4} $cm^2 \cdot V^{-1}$, over ten times higher than that of the control samples. Especially, the $\mu\tau$ product of the optimized highly textured single-crystal-like perovskite is even comparable to that of free-standing $MAPbBr_3$ single crystals[67,68]. With the fitting of the $\mu\tau$ product, we are able to estimate the total diffusion length and drift length L_d of the charge carrier in our optimized highly textured single-crystal $MAPbBr_3$, according to the equation: $L_d = \sqrt{\frac{k_B T}{q}\mu\tau} + \mu\tau\frac{V}{d}$, where k_B and T are Boltzmann constant and temperature, q and V are the elementary charge and bias voltage, and d is the thickness of perovskite layer, respectively[69]. After fitting, we show that L_d of the optimized highly textured single-crystal-like $MAPbBr_3$ could reach as high as 1,900 μm. Therefore, our optimized highly textured single-crystal-like $MAPbBr_3$ with a thickness of 145 μm is quite suitable for the charge carriers to penetrate perovskite single-crystal layers and reach the electrodes.

To investigate the photoresponse performance, we carried out the measurements on the current-voltage (*I-V*) curves of our photodiode devices based on the optimized highly textured single-crystal-like $MAPbBr_3$ in the dark and under illumination with different laser powers. As exhibited in Fig. 4(d), the photodiode device made by the optimized highly textured single-crystal-like $MAPbBr_3$ exhibits a high photocurrent of 2.4 × 10^{-7} A and an ultralow dark current of 8 × 10^{-11} A. Meanwhile, from Fig. 4(d), it can be found that the open-circuit voltage of our photodiode is about 1 V, indicating the built-in voltage is at least this value. Upon light illumination, the built-in voltage created from the junction would facilitate the photo-excited carrier separation and lead to a significant photodetection capability[70,71]. In comparison, as for the control device, the built-in voltage of the device is approximately 0.8 V (Fig. S9), less than that of the

optimized devices, which indicates less efficient charge separation. The difference between the two devices can be attributed to the improved material quality and optimized junction design in our device, which enhances the built-in voltage and overall photodiode operation. Notably, the asymmetric current curve indicates the typical behavior of the photodiode devices. Figure S10 shows the *I-V* curve in the linear scale in the dark condition. From this figure, the rectification ratio was calculated to be 33 at ±2 V. The ideality factor can be determined using the Schottky equation: $\ln(I) = \ln(I_0) + \frac{q}{kTn}V$, where I and I_0 are the diode current and reverse saturation current, respectively, while q and k stand for the electron charge and the Boltzmann constant[72]. At room temperature (T =300 K), the fitted ideality factor is 8.4. These values are consistent with literature reports, confirming the reasonable diode behavior of our photodiode devices[73–76]. In Fig. 4(e) and 4(f), we exhibited the transient photocurrent as a function of laser powers and the response times at a constant bias of 5 V and a laser illumination with a wavelength of 555 nm. Response time is defined as the necessary time required when the photocurrent rises from 10% to 90 % or falls from 90% to 10%. Both response times of our optimized highly textured single-crystal-like $MAPbBr_3$-based photodiodes are 45 ms, while the average response time of the control photodiodes is 236 ms, as shown in Fig. S11, which indicates the fast and sensitive features of our optimized highly textured single-crystal-like $MAPbBr_3$-based photodetection devices. Moreover, to evaluate the stability of our devices, we measured the response times of the devices fabricated using the optimized highly textured single-crystal-like $MAPbBr_3$ with different active areas. As shown in Fig. S12(a), the 6 × 5.5 cm^2 device exhibits an average response time of 43.5 ms, while the 2.5 × 3 cm^2 device displays a similar response time of 41.5 ms (Fig. S12(b)). These values are very close to those of our 10 × 10 cm^2 device, which indicates the consistent performance of the devices with different areas. The images of the highly textured single-crystal-like $MAPbBr_3$ films with areas of 6 × 5.5 cm^2 and 2.5 × 3 cm^2 are shown in Fig. S12(c). These comparable results further confirm the high stability of our devices fabricated using the modified ITC method. Additionally, the response time under self-powered operation was also examined, as shown in Fig. S13. It can be observed that our photodiode device exhibits the response times of τ_{rise} = 1.38 s and τ_{fall} = 103 ms at a 0 V bias, which are slower as compared to the biased situation. This demonstrates that under the external bias, charge carriers can be more rapidly separated and collected due to the enhanced electric field. In contrast, under self-powered conditions, the separation of photo-induced carriers can mainly rely on the built-in voltage; as a result, the carrier transport process is slower, leading to longer response times[77,78].

We further characterized the responsivity and detectivity of our photodiodes based on highly textured single-crystal-like perovskite films. The responsivity (R), indicating the strength of the photoresponse, can be calculated by the formula: $R = \frac{I_{light} - I_{dark}}{P}$, where I_{light} and I_{dark} are the current values upon light illumination and in the dark, respectively, while P is the laser power[79]. R provides a direct measure of the photodetection device's ability to convert incident light into an electrical signal. The specific detectivity (D^*), another critical parameter for photodetection devices, quantifies the sensitivity of the photodetectors to incident optical signals. It relates to both the responsivity and the noise characteristics of the devices. D^* can be defined by: $D^* = \frac{\sqrt{S\Delta f}}{I_{noise}}$, where S is the effective detection area, and Δf and I_{noise} stand for electrical bandwidth and total noise current, respectively[80]. As for halide perovskite materials, it is normally regarded that the dark currents are dominated by the shot noise[81]. In this regard, D^* can be expressed as: $D^* = \frac{R}{\sqrt{2qJ_d}}$, where q is the elemental charge, and J_d stands for dark current density[82]. From this equation, it can be clearly found that it is essential to minimize J_d values of the photodetectors to effectively distinguish weak optical signals. Our optimized highly textured single-crystal-like $MAPbBr_3$, characterized by low trap density and excellent optoelectronic properties, are advantageous for reducing leakage currents and noise levels during the device operation. Moreover, the photodiode device design with suitable interface layers working as photo-induced charge carrier transporting and blocking layers could futher reduce the dark current levels. Consequently, the devices achieve lower J_d, thereby improving the responsivity and detectivity values of the resulting devices. These attributes underscore the potential of highly textured single-crystal-like perovskites for high-performance photodetectors.

As shown in Fig. 5(a), we present the responsivity and specific detectivity of the optimized highly textured

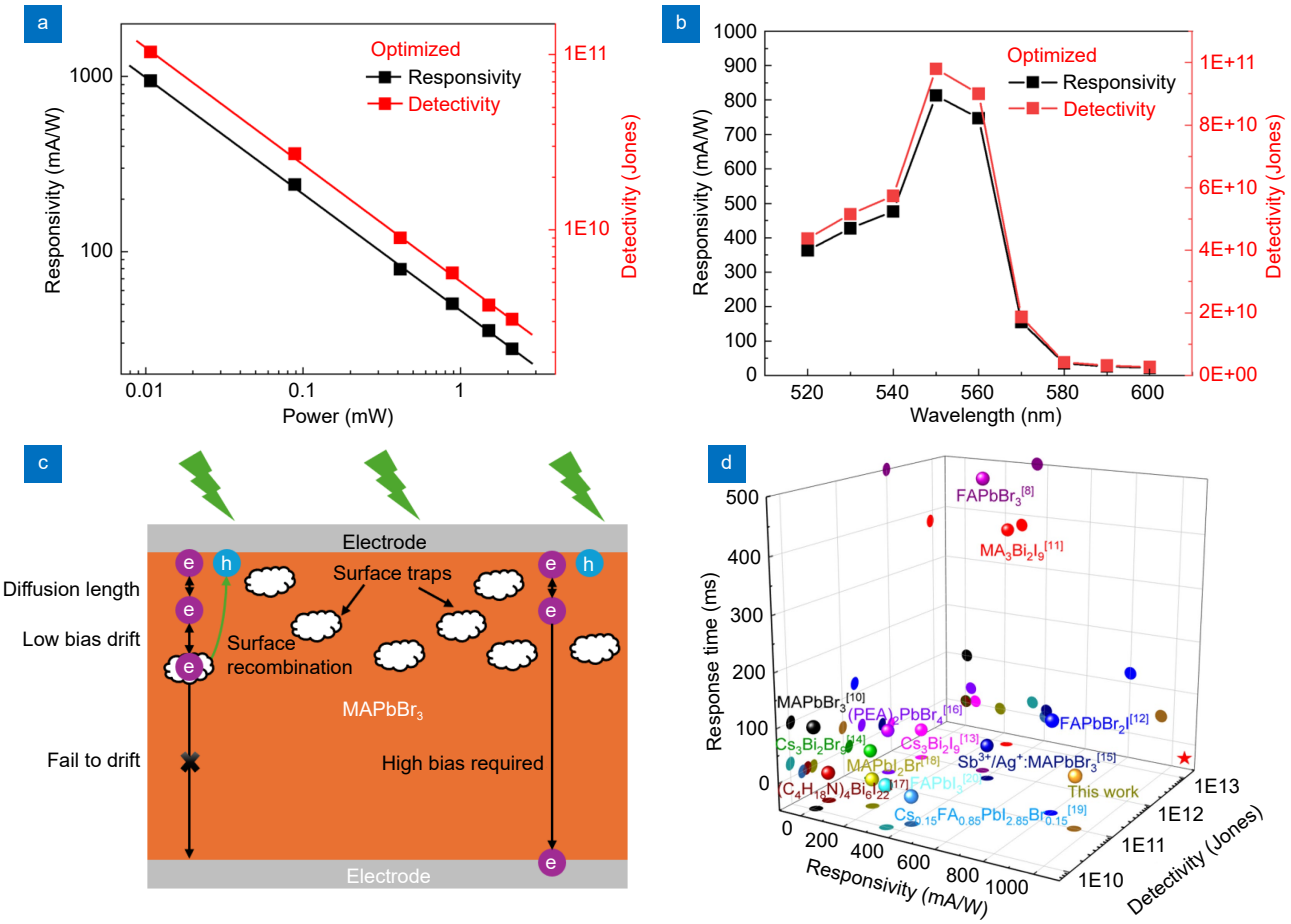

Fig. 5 | (**a**) Responsivity and detectivity of optimized highly textured single-crystal-like $MAPbBr_3$ photodiode under various laser powers with 555 nm wavelength at 5 V bias. (**b**) Responsivity and detectivity of the optimized device under various laser wavelengths. (**c**) Schematic illustration for the mechanism of narrowband detection enabled by surface charge recombination due to the surface traps. (**d**) Comparison of significant detection parameters between this work and other research works, including responsivity, detectivity, and response time, where the detailed information can be found in Tables S1 and S2 in the Supplementary information.

single-crystal-like $MAPbBr_3$ photodiode as a function of the light power, under a 555 nm laser and a 5 V bias. It can be observed the responsivity and specific detectivity considerably increase with the reduction of the laser power. When the laser power was reduced to 10 μW, the optimized highly textured single-crystal-like $MAPbBr_3$ photodiode presented a high responsivity of 944 $mA{\cdot}W^{-1}$ and also a satisfactory specific detectivity of approximately 1×10^{11} Jones. Meanwhile, we also evaluated the self-powered photodetection performance of the photodiode fabricated using our optimized highly textured single-crystal-like $MAPbBr_3$ film. Under a 0 V bias, the device exhibits a responsivity (R) of 0.2 mA/W and a detectivity (D^*) of 8.6×10^9 Jones, as derived from the data as shown in Fig. 4(d). Notably, previously reported self-powered photodiodes typically demonstrated the R values ranging from 10^0 to 10^1 mA/W and the D^* values on the order of approximately 10^9 Jones[83–87]. This indicates that our photodiode devices could show a clear self-powered photodetection capability, with performance metrics that can be comparable to or on par with those reported in the literature, also demonstrating the strong potential of our device for practical, bias-free photodetection applications. Notably, it is important to highlight that the quantum efficiency of photodiodes is restricted due to the different operating mechanisms of photodiodes and photoconductors. Specifically, in photoconductors, one type of carrier, such as holes, can be recirculated via symmetrical contacts before recombining with electrons. These carriers can remain trapped within the active layer of the photoconductor, resulting in high gain under such conditions[1]. While this high gain can enhance responsivity, photoconductors also exhibit notable drawbacks. For instance, their bandwidth is

typically limited due to the long carrier lifetimes required during the recirculation[88]. In contrast, photodiodes operate by separating photo-generated charge carriers using hole- and electron-transporting layers, which direct the carriers to opposite electrodes. This mechanism limits the quantum efficiency to a maximum of one, except in special cases involving carrier multiplication or avalanche effects, where values exceeding one can occur[89]. Therefore, with the restricted quantum efficiency, the responsivity of photodiodes could be lower than that of photoconductors.

In addition, the spectral responsivity and detectivity were also measured, of which the results are shown in Fig. 5(b). It can be clearly found that the sharp cut-down of both responsivity and detectivity can be observed after 560 nm, which matches the absorption feature and bandgap of $MAPbBr_3$ and verifies the photoresponse characteristic of the photodiodes. Moreover, a slight narrowband photoresponse near the absorption edge can be observed from both the spectral responsivity and detectivity curves, as shown in Fig. 5(b). This narrowband photoresponse feature can be attributed to the surface-charge recombination[54], and the schematic illustration is exhibited in Fig. 5(c) for the mechanism explanation. Due to the high absorption coefficient of the perovskite materials, the penetration depth of the laser is relatively limited for above-bandgap illumination, which leads to the charge carriers being generally excited within a shallow depth. In this case, these photo-excited charge carriers could be easily captured by the surface traps and annihilated because of the surface-charge recombination. Besides, the charge carriers with large mobility generated at shallow depths could diffuse to these surface-charge sinks quickly[90]. Consequently, the photoresponse from short wavelength areas will be weakened owing to the surface-charge recombination and further results in the narrowband photoresponse phenomenon from the spectra. However, light penetration could become deeper inside the crystal because of the smaller absorption coefficient when below-bandgap illumination is applied. These photo-induced carriers are more invulnerable to surface recombination because the applied bias voltage can propel carriers to another electrode before they diffuse back, which causes a higher charge collection efficiency. In this case, the photosensitive phenomenon can be more obvious at a longer wavelength range, consequently. Except for the optimized highly textured single-crystal-like $MAPbBr_3$ photodiodes, we also investigated the detection performance of the photodiode based on the control highly textured single-crystal-like $MAPbBr_3$. As shown in Fig. S14, the device based on the control highly textured single-crystal-like $MAPbBr_3$ presents unsatisfactory responsivity and detectivity values of only 173 $mA{\cdot}W^{-1}$ and $4.1{\times}10^9$ Jones, respectively, which are substantially lower than the optimized highly textured single-crystal-like $MAPbBr_3$ device, due to the poor crystallization conditions and flimsy contact at the interface without hot pressing. Therefore, the innovations we adopted are beneficial to achieve quick and sensitive detection of highly textured single-crystal-like $MAPbBr_3$ photodiodes. Furthermore, our photodiodes based on the optimized highly textured single-crystal-like $MAPbBr_3$ also exhibit excellent device stability. Figure S15 shows that the optimized photodiode device could still present over 80% photoresponsivity even after 2 months of storage, which matches the results of both XRD and PL analyses.

Achieving large-area photodetection using halide perovskite materials remains a significant challenge. Typically, photodetectors are limited to detecting objects with sizes comparable to the active area of the device, which constrains their applicability in real-world scenarios, despite otherwise excellent detection performance. In this work, we have successfully expanded the photodetection area to 100 cm^2 while maintaining competitive performance across key photodetection parameters, including responsivity, detectivity, and photoresponse speed. To underscore the competitiveness of our approach, particularly in the context of large-area detection, we present a comprehensive comparison in Table S1, summarizing the key performance metrics of halide perovskites reported in previous studies. Furthermore, Table S2 highlights the detection capabilities of various perovskite-based photodiodes, showcasing the substantial improvements achieved in our photodiodes. For a more intuitive comparison, we also visualize these performance parameters in a 3D coordinate plot (Fig. 5(d)), and the numbers from the superscript of each material are the corresponding references in the Supplementary information. In this plot, data points positioned nearer to the bottom-right corner, marked by a red star, indicate superior overall performance. Notably, our device is located closest to this benchmark, underscoring its outstanding performance among state-of-the-art halide perovskite photodiodes.

Particularly, it is worth highlighting that our solution-based process could have strong potential to be extended

to other types of halide perovskites. For example, successful fabrication of $CsPbBr_3$ film samples has been preliminarily achieved using a similar method, as shown in Fig. S16. While the synthesis of mixed-halide perovskites by this similar method has not yet been reported, we are optimistic about its feasibility. Given the similar structure and physical properties among various types of halide perovskites, we anticipate that this approach can be adapted to a wide range of perovskite systems, provided that appropriate experimental conditions, such as temperature and crystallization time, are carefully optimized. Meanwhile, the main limitation of this method could lie in the relatively complex growth requirements. For example, the regular monitoring and precise temperature control are essential, and additional post-treatments, such as hot pressing, may be necessary to achieve high-quality films.

Conclusions

In conclusion, we have developed a facile method for synthesizing large-area, highly textured single-crystal-like $MAPbBr_3$ films by integrating a modified ITC process with a hot-pressing treatment. These highly textured single-crystal-like perovskites were successfully employed as active light-absorbing layers in the fabrication of large-area, high-performance photodiode devices. Key factors contributing to the successful formation of these crystals include a controlled temperature gradient, induced perturbations, and the application of hot-pressing, all of which were essential for achieving uniform, large-area $MAPbBr_3$ single-crystal-like films with well-defined crystal orientation and strong interfacial contact with the substrate. The resulting single-crystal perovskites demonstrated outstanding material properties, including a large active area of approximately 100 cm^2, a low trap density of 1.4×10^{11} cm^{-3}, excellent carrier mobility of 217 $cm^2 \cdot V^{-1} \cdot s^{-1}$, and a high μτ product of 5.43×10^{-4} $cm^2 \cdot V^{-1}$. These attributes underscore the strong potential of our approach for scalable, high-performance photodetector applications.

Benefiting from the superior properties of the highly textured single-crystal-like active layers, alongside an optimized device architecture incorporating appropriate charge-transporting and blocking layers, the resulting photodiodes exhibit exceptional performance. These devices achieve a high responsivity of 944 $mA \cdot W^{-1}$, an optimal detectivity of up to 1×10^{11} Jones, and a fast photoresponse time of 45 ms within the visible spectrum. This cost-effective, solution-processed strategy enables the fabrication of large-area single-crystal-like perovskite photodiodes tailored to the size of target objects, thereby enhancing their suitability for practical applications. Overall, these findings demonstrate a scalable and affordable pathway for integrating perovskite single crystals into a broad range of commercial photodiode technologies, combining high performance with manufacturing viability.

Experimental section

Materials: methylammonium bromide (MABr, 99.9%) was purchased from Greatcell Solar Materials Pty Ltd. Lead bromide ($PbBr_2$, >98%), *N*,*N*-dimethylformamide (DMF, 99.8%), Poly(3,4-ethylenedioxythiophene)-poly(styrenesulfonate) (PEDOT:PSS), and Phenyl-C61-butyric acid methyl ester (PCBM) were purchased from Merck Life Science Pty Ltd. All commercial materials are used without any further purification.

Synthesis of highly textured single-crystal-like $MAPbBr_3$: the FTO/glass substrates in the crystallizing dish are rinsed and ultrasonicated sequentially with sufficient ethanol, acetone, and isopropanol for 10 min, and the FTO/glass substrates will be pre-treated by Plasma for 5 min to obtain the hydrophilic surface. PEDOT:PSS is filtered by a 0.22 μm filter and spin-coated on the FTO/glass substrate at 4000 rpm for 30 s, followed by annealing on a hot plate for 15 min at 135 °C. The same size filter is applied to filter the 0.75 M precursor solution of $MAPbBr_3$ in DMF, and the obtained solution is transferred to a crystallizing dish with FTO/glass substrates and a magnetic stirrer inside. The stirring plate is set at 150 rpm to introduce minor turbulence, and the temperature is elevated 5 °C every hour from 80 °C until the highly textured single-crystal-like perovskite is cohesive and covers all the FTO substrates. The substrates are taken out meticulously and annealed on a hot plate for 30 min at 100 °C, followed by hot pressing with a flat glass with a 2 kg weight on it for around 6 hours under 100 °C.

Device fabrication: to calculate trap density and carrier mobility, 5 nm Ti and 120 nm Au are deposited on the highly textured single-crystal-like $MAPbBr_3$ as electrodes. To fabricate the photodiode device, a 20 g/L solution of PCBM in Chlorobenzene is magnetically stirred at 60 °C for 3 hours. The obtained solution is spin-coated onto highly textured single-crystal-like halide perovskite at 1100 r.p.m for 30 s as an electron

transfer layer, and the device is annealed on a hot plate for 10 min at 100 °C. Eventually, 5 nm Ti and 120 nm Ag are deposited on the surface of the material successively. During the deposition process, the metal mask is used to create electrodes with 1 mm^2 as active areas of the photodiode device.

Characterization: the XRD pattern is analyzed by the Rigaku SmartLAB SE diffractometer. The surface morphology and cross-sectional thickness are obtained by scanning electron microscope (Zeiss EVO 50 SEM). The UV-Vis absorption spectra and steady-state photoluminescence were conducted by a spectrophotometer (Cary, Agilent) and a fluorescence spectrometer (DeltaFlex, HORIBA Scientific), respectively. The electrical properties of trap density, mobility, $\mu\tau$ product, and dark current are measured via recording the *I-V* curve by a Keithley 4200 Parameter analyzer (with probe station and light source).

Photodiode Characterization: the electrodes of Ti and Ag are thermally deposited by an E-beam Evaporator (AJA ATC-1800-E). To evaluate the performance of the detector, the 555 nm laser illumination is produced by a high-power supercontinuum white light laser (SuperK EVO, NKT Photonics) and a tunable wavelength filter with variable bandwidths (SuperK Varia, NKT Photonics). The laser instrument is controlled by the software. The powers of laser sources are adjusted by changing the output percentage and read through an optical power meter (PM100D, Thorlabs GmbH). Laser switching (on/off) was manually controlled through the software by clicking the "Power on" button. Meanwhile, the current density is recorded by a Keithley 4200 Parameter analyzer (with probe station) under a 5 V voltage bias to determine the responsivity, detectivity, and response time. The time resolution of the analyzer is about 10 ms.

References

1. García de Arquer FP, Armin A, Meredith P et al. Solution-processed semiconductors for next-generation photodetectors. *Nat Rev Mater* **2**, 16100 (2017).
2. Liu RK, Li F, Zeng F et al. Halide perovskite x-ray detectors: fundamentals, progress, and outlook. *Appl Phys Rev* **11**, 021327 (2024).
3. Qadir A, Shafique S, Iqbal T et al. Recent advancements in polymer-based photodetector: a comprehensive review. *Sens Actuators A Phys* **370**, 115267 (2024).
4. Xin W, Zhong WH, Shi YJ et al. Low-dimensional-materials-based photodetectors for next-generation polarized detection and imaging. *Adv Mater* **36**, 2306772 (2024).
5. Xu YL, Lin QQ. Photodetectors based on solution-processable semiconductors: recent advances and perspectives. *Appl Phys Rev* **7**, 011315 (2020).
6. Zhang XR, Jiang JZ, Feng BG et al. Organic photodetectors: materials, device, and challenges. *J Mater Chem C* **11**, 12453–12465 (2023).
7. Wang YM, Li M, Chai ZF et al. Perovskite scintillators for improved X-ray detection and imaging. *Angew Chem Int Ed* **62**, e202304638 (2023).
8. Zhao X, Lu HR, Fang WH et al. Correlated organic-inorganic motion enhances stability and charge carrier lifetime in mixed halide perovskites. *Nanoscale* **14**, 4644–4653 (2022).
9. Tong Y, Najar A, Wang L et al. Wide-bandgap organic-inorganic lead halide perovskite solar cells. *Adv Sci* **9**, 2105085 (2022).
10. Geng XS, Chen YA, Li YY et al. Lead-free halide perovskites for direct X-ray detectors. *Adv Sci* **10**, 2300256 (2023).
11. Zheng DM, Pauporté T. Advances in optical imaging and optical communications based on high-quality halide perovskite photodetectors. *Adv Funct Mater* **34**, 2311205 (2024).
12. Moon J, Mehta Y, Gundogdu K et al. Metal-halide perovskite lasers: cavity formation and emission characteristics. *Adv Mater* **36**, 2211284 (2024).
13. Liu YR, Liu YQ, Guo YL. Organic-inorganic hybrid perovskite materials and their application in transistors. *Mater Chem Front* **7**, 5215–5246 (2023).
14. Dong X, Shen Y, Wang FM et al. $MAPbX_3$ perovskite single crystals for advanced optoelectronic applications: progress, challenges, and perspective. *Small* **21**, 2412809 (2025).
15. Liu YC, Yang Z, Cui D et al. Two-inch-sized perovskite $CH_3NH_3PbX_3$ (X= Cl, Br, I) crystals: growth and characterization. *Adv Mater* **27**, 5176–5183 (2015).
16. Hsu HP, Li LC, Shellaiah M et al. Structural, photophysical, and electronic properties of $CH_3NH_3PbCl_3$ single crystals. *Sci Rep* **9**, 13311 (2019).
17. Li JY, Gu Y, Han ZY et al. Further advancement of perovskite single crystals. *J Phys Chem Lett* **13**, 274–290 (2022).
18. Song YL, Wang LX, Shi YQ et al. Detector-grade perovskite single-crystal wafers via stress-free gel-confined solution growth targeting high-resolution ionizing radiation detection. *Light Sci Appl* **12**, 85 (2023).
19. Zheng XJ, Zhao W, Wang P et al. Ultrasensitive and stable X-ray detection using zero-dimensional lead-free perovskites. *J Energy Chem* **49**, 299–306 (2020).
20. Li HY, Shen N, Chen S et al. Recent progress on synthesis, intrinsic properties and optoelectronic applications of perovskite single crystals. *Adv Funct Mater* **33**, 2214339 (2023).
21. Li YH, Gui PB, Wei SY et al. Template-assisted synthesis of 2D perovskite grating single crystal films at low temperatures for UV polarization-sensitive photodetectors. *Small* **20**, 2305207 (2024).
22. Lou YJ, Zhang SS, Gu ZK et al. Perovskite single crystals: dimensional control, optoelectronic properties, and applications. *Mater Today* **62**, 225–250 (2023).
23. Zhang JS, Song JP, Zhang Q. Large-scale perovskite single crystal growth and surface patterning technologies. *Small Sci* **3**, 2300085 (2023).
24. Saidaminov MI, Adinolfi V, Comin R et al. Planar-integrated single-crystalline perovskite photodetectors. *Nat Commun* **6**, 8724 (2015).
25. Li DW, Chen YT, Tang YJ et al. Solution-processed organic-inorganic semiconductor heterostructures for advanced hybrid phototransistors. *ACS Appl Electron Mater* **5**, 578–592 (2023).
26. Chen FT, Li CQ, Shang CY et al. Ultrafast response of centimeter scale thin $CsPbBr_3$ single crystal film photodetector for

optical communication. *Small* **18**, 2203565 (2022).
27. Liu YC, Zhang YX, Zhu XJ et al. Inch-sized high-quality perovskite single crystals by suppressing phase segregation for light-powered integrated circuits. *Sci Adv* **7**, eabc8844 (2021).
28. Zhang HJ, Liu X, Dong JP, et al. Centimeter-sized inorganic lead halide perovskite $CsPbBr_3$ crystals grown by an improved solution method. *Cryst Growth Des* **17**, 6426–6431 (2017).
29. Zhang XY, Ji CM, Liu XT et al. Solution-grown large-sized single-crystalline 2D/3D perovskite heterostructure for self-powered photodetection. *Adv Opt Mater* **8**, 2000311 (2020).
30. Zia W, Aranda CA, Pospisil J et al. Impact of low-temperature seed-assisted growth on the structural and optoelectronic properties of $MAPbBr_3$ single crystals. *Chem Mater* **35**, 5458–5467 (2023).
31. Xing J, Zou Y, Zhao C et al. Thickness-dependent carrier lifetime and mobility for $MAPbBr_3$ single crystals. *Mater Today Phys* **14**, 100240 (2020).
32. Su J, Sang L, Wang D et al. Solution growth and morphology of $CH_3NH_3PbBr_3$ single crystals in different solvents. *Cryst Res Technol* **51**, 650–655 (2016).
33. Su CH. A method of promoting single crystal yield during melt growth of semiconductors by directional solidification. *J Cryst Growth* **410**, 35–38 (2015).
34. Liao MQ, Xia ML, Xu YS et al. Growth mechanism of metal halide perovskite single crystals in solution. *Chem Commun* **59**, 8758–8768 (2023).
35. Yan JK, Li HJ, Aldamasy MH et al. Advances in the synthesis of halide perovskite single crystals for optoelectronic applications. *Chem Mater* **35**, 2683–2712 (2023).
36. Chen GY, Liu XY, An JK et al. Nucleation-mediated growth of chiral 3D organic-inorganic perovskite single crystals. *Nat Chem* **15**, 1581–1590 (2023).
37. Liu D, Jiang L, Jiang XY et al. Interface-tension-assisted temperature-gradient crystallization of high-quality $MAPbBr_3$ perovskite single crystals with low defect densities. *ACS Appl Mater Interfaces* **15**, 57846–57855 (2023).
38. Liu YC, Zhang YX, Yang Z et al. Low-temperature-gradient crystallization for multi-inch high-quality perovskite single crystals for record performance photodetectors. *Mater Today* **22**, 67–75 (2019).
39. Sung MH, Kim JS, Kim WS et al. Modification of crystal growth mechanism of yttrium oxalate in metastable solution. *J Cryst Growth* **235**, 529–540 (2002).
40. Li N, Li YY, Xie SD et al. High-performance and self-powered X-ray detectors made of smooth perovskite microcrystalline films with 100 μm grains. *Angew Chem* **135**, e202302435 (2023).
41. Wu G, Cai ML, Cao YJ et al. Enlarging grain sizes for efficient perovskite solar cells by methylamine chloride assisted recrystallization. *J Energy Chem* **65**, 55–61 (2022).
42. Zhai P, Ren LX, Zhang YR et al. Performance-limiting formation kinetics in green water-processed perovskite solar cells. *Energy Environ Sci* **16**, 3014–3024 (2023).
43. Wang T, Lian G, Huang LP et al. A crystal-growth boundary-fusion strategy to prepare high-quality $MAPbI_3$ films for excellent Vis-NIR photodetectors. *Nano Energy* **64**, 103914 (2019).
44. Xiao JY, Yang YY, Xu X et al. Pressure-assisted $CH_3NH_3PbI_3$ morphology reconstruction to improve the high performance of perovskite solar cells. *J Mater Chem A* **3**, 5289–5293 (2015).
45. Andrade PHM, Volkringer C, Loiseau T et al. Band gap analysis in MOF materials: distinguishing direct and indirect transitions using UV-vis spectroscopy. *Appl Mater Today* **37**, 102094 (2024).
46. Liu D, Wu JL, Lu YB et al. 3D digital holography investigations of giant photostriction effect in $MAPbBr_3$ perovskite single crystals. *Adv Funct Mater* **34**, 2404995 (2024).
47. Sauer M, Hofkens J, Enderlein J. *Handbook of Fluorescence Spectroscopy and Imaging: from Ensemble to Single Molecules* (Wiley-VCH, Weinheim & Sons, 2011).
48. Guo XB, Li N, Xu YS et al. Mitigating surface deficiencies of perovskite single crystals enables efficient solar cells with enhanced moisture and reverse-bias stability. *Adv Funct Mater* **33**, 2213995 (2023).
49. He TW, Li SS, Jiang YZ et al. Reduced-dimensional perovskite photovoltaics with homogeneous energy landscape. *Nat Commun* **11**, 1672 (2020).
50. Le Corre VM, Duijnstee EA, Tambouli OE et al. Revealing charge carrier mobility and defect densities in metal halide perovskites via space-charge-limited current measurements. *ACS Energy Lett* **6**, 1087–1094 (2021).
51. Maggiora J, Li F, Zheng RK. Charge transport properties of methylammonium lead trihalide hybrid perovskite bulk single crystals. *Phys Status Solidi Rapid Res Lett* **15**, 2000410 (2021).
52. Youn SSO, Kim GY, Jo W. Structural modifications due to Bi-doping in $MAPbBr_3$ single crystals and their impact on electronic transport and stability. *Small* **20**, 2407141 (2024).
53. Wang CQ, Chen S, Jie JS et al. Metal halide perovskite single crystals toward electroluminescent applications. *Adv Funct Mater* **35**, 2401189 (2025).
54. Shi D, Adinolfi V, Comin R et al. Low trap-state density and long carrier diffusion in organolead trihalide perovskite single crystals. *Science* **347**, 519–522 (2015).
55. Liu Y, Zheng XP, Fang YJ et al. Ligand assisted growth of perovskite single crystals with low defect density. *Nat Commun* **12**, 1686 (2021).
56. Yuan JF, Zhang D, Deng BB et al. High efficiency inorganic perovskite solar cells based on low trap density and high carrier mobility $CsPbI_3$ films. *Adv Funct Mater* **32**, 2209070 (2022).
57. Wetzelaer GJAH, Scheepers M, Sempere AM et al. Trap-assisted non-radiative recombination in organic-inorganic perovskite solar cells. *Adv Mater* **27**, 1837–1841 (2015).
58. Cheng PH, Chen Q, Liu HY et al. Exploration of conjugated π-bridge units in *N, N*-bis (4-methoxyphenyl) naphthalen-2-amine derivative-based hole transporting materials for perovskite solar cell applications: a DFT and experimental investigation. *RSC Adv* **12**, 1011–1020 (2022).
59. Mehdi H, Mhamdi A, Hannachi R et al. $MAPbBr_3$ perovskite solar cells *via* a two-step deposition process. *RSC Adv* **9**, 12906–12912 (2019).
60. Pan MA, Lau TK, Tang YB et al. 16.7%-efficiency ternary blended organic photovoltaic cells with PCBM as the acceptor additive to increase the open-circuit voltage and phase purity. *J Mater Chem A* **7**, 20713–20722 (2019).
61. Attia A, Fatima M, Khan MI et al. Revolutionizing perovskite solar cells: enhancing current density through Zr doping in $MAPbBr_3$ to engineer shifted band gap edges near the electron transport layer. *Opt Mater* **145**, 114419 (2023).
62. Kong TF, Song J, Zhang Y et al. A newly crosslinked-double network PEDOT: PSS@PEGDMA toward highly-efficient and stable tin-lead perovskite solar cells. *Small* **19**, 2303159 (2023).
63. Sánchez JG, Cabrera-Espinoza A, Martínez-Ferrero E et al. Chalcogen-substituted PCBM derivatives as ternary components in PM6: Y6 solar cells. *Mater Adv* **3**, 1071–1078 (2022).
64. Wang H, Wang P, Sun YD et al. Photoconductive charge transfer complexes as charge transport layers for high performance

inverted perovskite solar cells. *Adv Funct Mater* **32**, 2201935 (2022).
65. Whitten JE. Ultraviolet photoelectron spectroscopy: practical aspects and best practices. *Appl Surf Sci Adv* **13**, 100384 (2023).
66. Pan L, Liu ZF, Welton C et al. Ultrahigh-flux X-ray detection by a solution-grown perovskite $CsPbBr_3$ single-crystal semiconductor detector. *Adv Mater* **35**, 2211840 (2023).
67. Luo XT, Gao L, Sun JL et al. X-ray irradiation fluence-dependent carrier transport capacity of $MAPbBr_3$ single crystal. *Adv Opt Mater* **12**, 2302396 (2024).
68. Zhang XJ, Chu DP, Jia BX et al. Heterointerface design of perovskite single crystals for high-performance X-ray imaging. *Adv Mater* **36**, 2305513 (2024).
69. Olschner F, Toledo-Quinones M, Shah KS et al. Charge carrier transport properties in thallium bromide crystals used as radiation detectors. *IEEE Trans Nucl Sci* **37**, 1162–1164 (1990).
70. Xu YL, Li W, Yu T et al. Pulsed-laser detectors based on metal halide perovskites. *Laser Photonics Rev* **15**, 2100169 (2021).
71. Liu SL, Chen Y, Gao WQ et al. Epitaxy of a monocrystalline $CsPbBr_3$–$SrTiO_3$ halide-oxide perovskite p-n heterojunction with high stability for photodetection. *Adv Mater* **35**, 2303544 (2023).
72. Zhang LX, Chen HX, Guo LY et al. Dual defect passivation engineering of perovskite photodetectors toward infrared filter-free full-color imaging. *Adv Opt Mater* **13**, e01861 (2025).
73. Zhao YP, Zhang ZH, Yan SS et al. A photo-switchable rectifier based on the $MAPbBr_3$-$MAPbCl_3$ halide perovskite heterostructure for dual-wavelength optical communications. *J Mater Chem C* **11**, 11697–11704 (2023).
74. Hedzir AS, Hasbullah NF. A review of high ideality factor in gallium nitride-based light-emitting diode. *Semicond Phys Quantum Electron Optoelectron* **24**, 83–89 (2021).
75. Rajeswari R, Venugopal D, George A et al. Design, construction and performance of P-N junction diode prepared with Fe-TiO_2 thin films. *Mater Lett* **281**, 128604 (2020).
76. Chatterjee K, Nayak M, Akhtar AJ et al. Sn doping enhanced current rectification in $MAPbBr_3$ nanocrystal-metal junction for photodetection. *Mater Today: Proc* **66**, 3205–3210 (2022).
77. Zhang JN, Feng XF, Mei LY et al. A $MAPbBr_3/PdSe_2$ Schottky junction-based optoelectronic sensor with self-powered and switchable photocurrents. *Mater Des* **234**, 112368 (2023).
78. Yao JF, Zhang H, Lu JZ et al. A self-power photodetector based on controlled growth of single crystal $MAPbBr_3/WO_3$ heterojunction. *Sci China Technol Sci* **66**, 2660–2668 (2023).
79. Wu WQ, Lu H, Han X et al. Recent progress on wavelength-selective perovskite photodetectors for image sensing. *Small Methods* **7**, 2201499 (2023).
80. Wang F, Zou XM, Xu MJ et al. Recent progress on electrical and optical manipulations of perovskite photodetectors. *Adv Sci* **8**, 2100569 (2021).
81. He LJ, Wang DY, Zhao Y et al. Efficient hole transport layers based on cross-linked poly (*N*-vinylcarbazole) for high-performance perovskite photodetectors. *J Mater Chem C* **9**, 11722–11728 (2021).
82. Guo ZY, Zhang JY, Liu X et al. Optoelectronic synapses and photodetectors based on organic semiconductor/halide perovskite heterojunctions: materials, devices, and applications. *Adv Funct Mater* **33**, 2305508 (2023).
83. Pramod AK, Subramaniam MR, Hevia SA et al. Synthesis of lead-free $Cs_3Sb_2Cl_3Br_6$ halide perovskite through solution processing method for self-powered photodetector applications. *Mater Lett* **306**, 130874 (2022).
84. Chen YH, Feng ZJ, Pal A et al. Recent progress on the performance of lead-based halide perovskite $APbX_3$ detectors. *Phys Status Solidi A Appl Mater Sci* **219**, 2200018 (2022).
85. Zhu YF, Song ZH, Zhou H et al. Self-powered, broadband perovskite photodetector based on ZnO microspheres as scaffold layer. *Appl Surf Sci* **448**, 23–29 (2018).
86. Li S, Wang FY, Dong SH et al. Sizeable square $CsPb_2Br_5$ nanosheets for photodetection. *Chem Commun* **60**, 4679–4682 (2024).
87. Dhakshnamoorthy M, Kathirvel A, Raj SM et al. Self-powered white light photodetector with enhanced photoresponse using camphor sulphonic acid treated $CsPbBr_3$ perovskite in carbon matrix. *Mater Lett* **341**, 134250 (2023).
88. Petritz RL. Theory of photoconductivity in semiconductor films. *Phys Rev* **104**, 1508–1516 (1956).
89. Konstantatos G, Sargent EH. Nanostructured materials for photon detection. *Nat Nanotechnol* **5**, 391–400 (2010).
90. Fang YJ, Dong QF, Shao YC et al. Highly narrowband perovskite single-crystal photodetectors enabled by surface-charge recombination. *Nat Photonics* **9**, 679–686 (2015).

Acknowledgements

The authors acknowledge the financial support from the University of Sydney International Stipend Scholarship and the University of Sydney Tuition Fee Scholarship.
The authors acknowledge the support of The University of Sydney Physics Foundation as well as the facilities and technician assistance from the Sydney Microscopy & Microanalysis, Sydney Analytical, and Research Prototype & Foundry at The University of Sydney.

Competing interests

The authors declare no competing financial interests.

Data availability

The data that support the findings of this study are available from the corresponding author upon reasonable request.

Supplementary information

Supplementary information for this paper is available at
https://doi.org/10.29026/oea.2025.250168

Scan for Article PDF